Reversible and nonvolatile ferroelectric control of two-dimensional electronic transport properties of ZrCuSiAs-type copper oxyselenide thin films with a layered structure

Xu-Wen Zhao,[1] Guan-Yin Gao,[2] Jian-Min Yan,[1] Lei Chen,[1] Meng Xu,[1] Wei-Yao Zhao,[1] Zhi-Xue Xu,[1] Lei Guo,[1] Yu-Kuai Liu,[3,*] Xiao-Guang Li,[2] Yu Wang,[4,*] and Ren-Kui Zheng[1,4,*]

[1]*State Key Laboratory of High Performance Ceramics and Superfine Microstructure, Shanghai Institute of Ceramics, Chinese Academy of Sciences, Shanghai 200050, China*

[2]*Hefei National Laboratory for Physical Sciences at the Microscale, Department of Physics, and Collaborative Innovation Center of Advanced Microstructures, University of Science and Technology of China, Hefei 230026, China*

[3]*Department of Applied Physics, The Hong Kong Polytechnic University, Hong Kong, China*

[4]*School of Materials Science and Engineering, Nanchang University, Nanchang 330031, China*

(Received 29 January 2018; published 24 May 2018)

Copper-based ZrCuSiAs-type compounds of LnCuChO (Ln = Bi and lanthanides, Ch = S, Se, Te) with a layered crystal structure continuously attract worldwide attention in recent years. Although their high-temperature ($T \geqslant 300$ K) electrical properties have been intensively studied, their low-temperature electronic transport properties are little known. In this paper, we report the integration of ZrCuSiAs-type copper oxyselenide thin films of $Bi_{0.94}Pb_{0.06}CuSeO$ (BPCSO) with perovskite-type ferroelectric $Pb(Mg_{1/3}Nb_{2/3})O_3$-$PbTiO_3$ (PMN-PT) single crystals in the form of ferroelectric field effect devices that allow us to control the electronic properties (e.g., carrier density, magnetoconductance, dephasing length, etc.) of BPCSO films in a reversible and nonvolatile manner by polarization switching at room temperature. Combining ferroelectric gating and magnetotransport measurements with the Hikami-Larkin-Nagaoka theory, we demonstrate two-dimensional (2D) electronic transport characteristics and weak antilocalization effect as well as strong carrier-density-mediated competition between weak antilocalization and weak localization in BPCSO films. Our results show that ferroelectric gating using PMN-PT provides an effective and convenient approach to probe the carrier-density-related 2D electronic transport properties of ZrCuSiAs-type copper oxyselenide thin films.

DOI: 10.1103/PhysRevMaterials.2.055003

I. INTRODUCTION

The quaternary 1111 phases with a layered crystal structure of the ZrCuSiAs-type form a broad family of materials including iron-based superconductors (e.g., $LaFeAsO_{1-x}F_x$) [1], optoelectronic chalcogenide semiconductors [e.g., LnCuChO [2,3], (Ln = lanthanides, Ch = S, Se, Te)], magnetic gapless semimetals (e.g., $YZn_{0.89}Co_{0.11}AsO$) [4], ferromagnetic Kondo lattice systems (e.g., CeRuPO) [5], bipolar magnetic semiconductors (e.g., La(Mn,Zn)AsO) [6], etc., and have been attracting increasing worldwide interest in recent years. As a member of this vast family, divalent element-doped BiCuSeO (BCSO) semiconducting compounds show the highest thermoelectric performance (figure of merit $ZT \sim 1.4$ @ 923 K [7]) among oxygen containing materials and a high flexibility to element doping (e.g., Ca, Sr, Ba, Pb, S, Te), which modifies the carrier density and band gap and hence enhances the electrical conductivity and thermoelectric properties [7–10]. Indeed, the element doping is an effective and convenient strategy for tuning the carrier density and its related physical properties of BCSO compounds. This approach, however, inevitably brings about additional lattice distortion, disorders, defects, and/or secondary phases, etc., which is discouraging from fundamental research perspectives. To better understand the important role played by the carrier density in this class of copper oxyselenides, it is necessary to *in situ* tune and modulate the carrier density in a reversible and nonvolatile manner without element doping.

Electric-field-controllable electrostatic tuning of carrier density offers a unique opportunity to probe the carrier-density-related physical properties of a variety of functional thin films [11–17]. Since the volume carrier density of divalent element-doped BCSO is relatively large ($n_{3D} \sim 10^{20}\,cm^{-3}$ [7–9,18], or $n_{2D} \sim 10^{14}\,cm^{-2}$ for a 10-nm-thick film), it is a great challenge to tune their carrier density effectively using the widely used dielectric gate materials such as the SiO_2, Al_2O_3, HfO_2, *h*-BN, SiN_x, and $SrTiO_3$ because the electric-field-induced areal polarization charges by these gate materials are not only volatile but also too small ($\sim 10^{12}-10^{13}\,cm^{-2}$) (see Ref. [19] for more details). In this context, we note that the perovskite $Pb(Mg_{1/3}Nb_{2/3})O_3$-$PbTiO_3$ (PMN-PT) single crystals possess excellent ferroelectric properties at room temperature, which can be exploited for realizing reversible and nonvolatile tuning of carrier density of films [13,14]. They have a large nonvolatile remnant polarization of $2P_r \sim 50-60\,\mu C/cm^2$ [13,16], which corresponds to an areal charge density of $\sim 3.1-3.7 \times 10^{14}/cm^2$. This value is comparable to the carrier density of divalent element-doped BCSO and at least, one order of magnitude higher than what could be achieved by using the above mentioned dielectric gate materials. Moreover,

*Corresponding authors: liuyk@mail.ustc.edu.cn; wangyu@ncu.edu.cn; zrk@ustc.edu

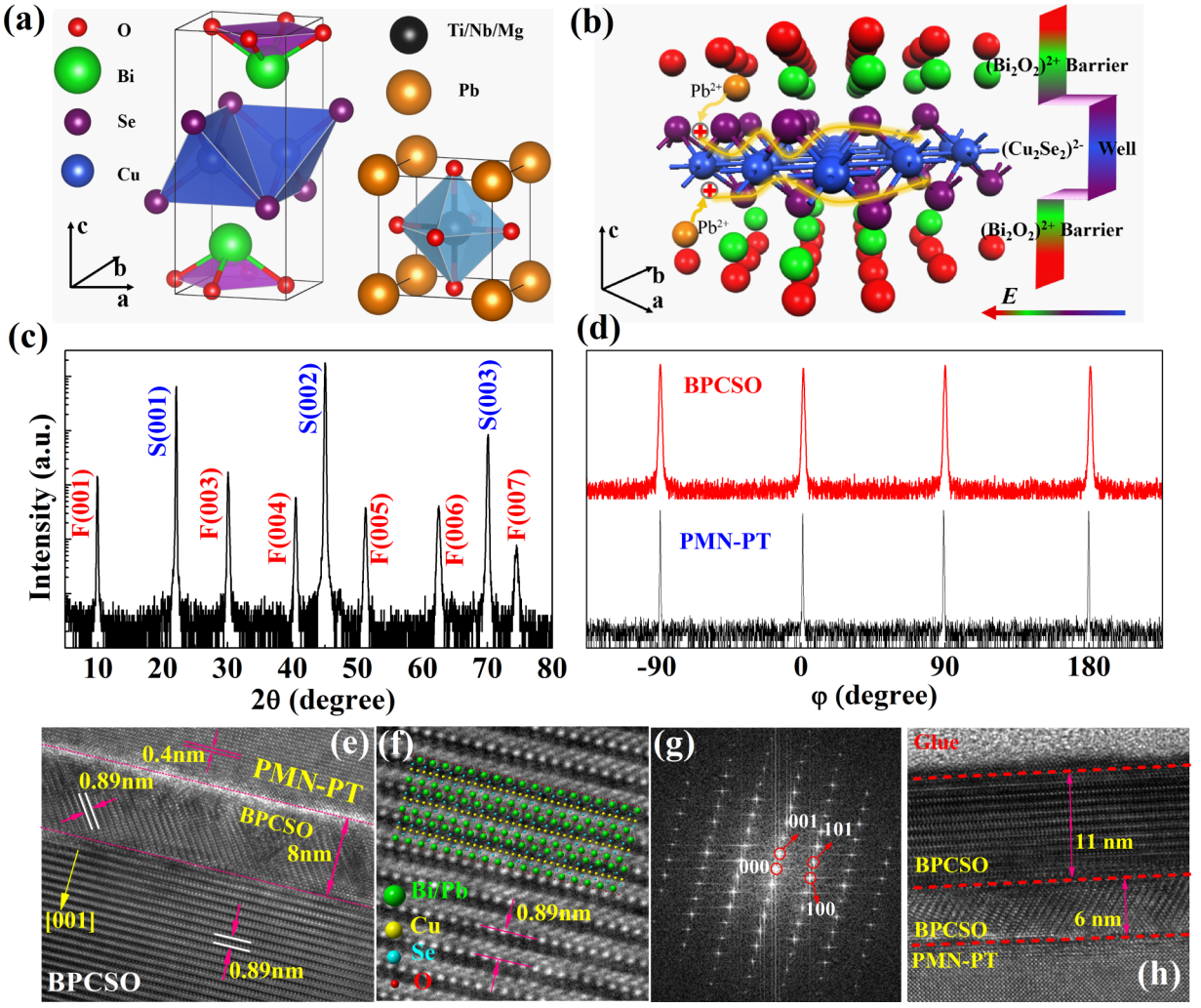

FIG. 1. Structure characterization of BPCSO films. (a) Crystal structures of BPCSO and PMN-PT. (b) Schematic illustration of the natural multiple quantum well structure of the layered BPCSO. (c) Out-of-plane XRD θ-2θ scan pattern of a BPCSO(160-nm)/PMN-PT structure. (d) ϕ-scan patterns of the BPCSO(160-nm)/PMN-PT structure. (e) Cross-sectional TEM image of a 160-nm BPCSO film. (f) An enlarged TEM image taken from (e). (g) Power spectrum of the fast Fourier transform of (e). (h) Cross-sectional TEM image of the ~16-nm BPCSO film.

PMN-PT single crystals have pseudocubic perovskite structures whose lattice parameters a and b ($a \sim b \sim c \sim 4.02$ Å) are slightly larger than those of the BCSO ($a = b = 3.9273$ Å, $c = 8.9293$ Å, space group *P4/nmm*), making them still suitable substrates for the epitaxial growth of BCSO-based films.

Similar to LnCuChO compounds [3,20], the two-dimensional (2D) layered BCSO can be viewed as natural multiple quantum wells (NMQWs) built into its layered structure in which the $(Bi_2O_2)^{2+}$ insulating layers act as inherent blocking barriers for the carriers' motion along the c axis, while the $(Cu_2Se_2)^{2-}$ layers act as the carrier conducting layers [Figs. 1(a) and 1(b)]. Many experimental works have shown that the replacement of a small portion of Bi atoms (~6%) by Pb atoms significantly enhances the carrier density, electrical conductivity, and thermoelectric performance because of the release of hole carriers from the $(Bi_2O_2)^{2+}$ charge reservoir layers to the $(Cu_2Se_2)^{2-}$ conducting layers [8]. Therefore, in this paper, we fabricated $Bi_{0.94}Pb_{0.06}CuSeO$(BPCSO)/PMN-PT ferroelectric field effect transistor (FeFET) devices by growing BPCSO films on ferroelectric PMN-PT (001) single-crystal substrates. We realized reversible and nonvolatile electric-field control of the carrier density and related electronic transport properties of BPSCO films through polarization switching at room temperature and observed strong anisotropic magnetotransport behaviors and sharp cusps in the magnetoconductance versus magnetic field curves within low-field region, which is a signature of the weak antilocalization (WAL) effect. We also found carrier-density-mediated strong competition between the WAL and the weak localization (WL). Our results offer a more in-depth understanding of the low-temperature electronic properties of BCSO-based films, which is rarely studied and little known as of now.

II. EXPERIMENTAL DETAILS

PMN-PT single crystals with a large size of Φ 75 mm × 700 mm were grown by the modified Bridgeman technique at the Shanghai Institute of Ceramics. The crystals were cut

into small pieces with a size of 5 mm [100] × 5 mm [010] × 0.5 mm [001] and carefully polished to a root-mean-square roughness less than 1 nm. BPCSO thin films were grown on one-side polished PMN-PT (001) single-crystal substrates by pulsed laser deposition (PLD) from a high-purity BPCSO target prepared by spark plasma sintering for 8 min under 50 MPa at 700 °C. The target was ablated by a KrF excimer laser (248 nm) with a pulse energy density of 1.2 J/cm^2 and a repetition rate of 2 Hz. The film deposition was carried out under 1-Pa Ar atmosphere and a substrate temperature of 450 °C, followed by *in situ* annealing for 30 min and cooled to room temperature at a rate of 5 °C/min.

Structural properties of BPCSO thin films were characterized by a high-resolution four-circle Bruker D8 Discover x-ray diffractometer using Cu $K_{\alpha 1}$ radiation ($\lambda = 1.5406$ Å) and a high-resolution transmission electron microscope (Tecnai G2 F20 S-Twin). The in-plane electronic transport properties of BPCSO films were measured in the temperature range from 2 to 300 K using a Physical Property Measurement System (PPMS-9, Quantum Design). Using the conducting BPCSO film and the Ag film (∼100 nm) as the top and bottom electrodes, respectively, the poling of PMN-PT substrates were achieved by applying a positive or negative dc voltage of 330 V (∼6.6 kV/cm) to the PMN-PT along the thickness direction. We particularly note here that all electronic transport measurements were made after the 330-V dc poling voltage had been turned off.

The magnetic hysteresis loops of BPCSO films were measured using Quantum Design MPMS XL-5 SQUID Magnetometer. The polarization-electric field hysteresis loops were measured using a Precision Multiferroic ferroelectric analyzer (Radiant Technologies, Inc. USA). The piezoresponse force microscopy images were measured using the MFP-3D Infinity atomic force microscope (Oxford Instruments Asylum Research Inc.).

III. RESULTS AND DISCUSSION

Figure 1(c) shows the XRD θ-2θ linear scan pattern of a thick BPCSO(160-nm)/PMN-PT structure. Except the peaks from the PMN-PT substrate, only BPCSO (00l) (l = 1, 3, 4, 5, 6, 7) diffraction peaks can be observed, indicating that the BPCSO film is single phase and preferentially oriented along the c axis. The lattice parameter c is determined to be 8.91 Å, slightly smaller than that of the BCSO parent compound. The full width at half maximum of the rocking curve taken on the BPCSO (003) diffraction peak exhibits a value of 1° (see Ref. [19]). XRD ϕ scans were employed to understand the in-plane lattice arrangement between the BPCSO and the PMN-PT. As shown in Fig. 1(d), both the ϕ-scan peaks taken on the (102) reflection of the BPCSO film and the (101) reflection of the PMN-PT substrate exhibit four-fold symmetry with 90° intervals and appear at the same azimuth angles, which suggests that the BPCSO film is probably epitaxially grown on the PMN-PT substrate. To further characterize the structural properties, we performed high-resolution transmission electron microscopy (HRTEM) measurements. Figure 1(e) shows a cross-sectional HRTEM image taken near the interface region of a thick BPCSO(160-nm)/PMN-PT structure. Unexpectedly, the image shows that there is a ∼8-nm BPCSO interface layer whose c axis tilts by approximately 55° with respect to the substrate plane while the remaining part of the film grows layer by layer along the c axis (see Ref. [19]). The interlayer distance is approximately 0.89 nm, which matches well with that of the (001) plane of the BPCSO and is consistent with that obtained from the XRD result. Figure 1(f) shows an enlarged HRTEM image whose atomic arrangement is consistent with the simulation of ZrCuSiAs-type structural model. The electron diffraction pattern produced by fast Fourier transform (FFT) of the lattice image shown in Fig. 1(e) coincides with the simulated diffraction pattern along the [010] zone axis of the BPCSO (see Ref. [19]). HRTEM images of the ∼16-nm BPCSO film [Fig. 1(h)] also exhibit a ∼6-nm interface layer whose c axis tilts by ∼55° with respect to the substrate plane while the remaining part of the film grows layer by layer along the c axis.

We constructed BPCSO/PMN-PT semiconductor/ferroelectrics devices based on the concept of ferroelectric field effect. The application of an electric field (E field) with upward direction to the PMN-PT induces negative polarization charges on the surface of PMN-PT, which would attract positive screening charges (i.e., holes) from the BPCSO films. As a result, the BPCSO film would be depleted from hole carriers, as schematically illustrated in Fig. 2(a). In contrast, the application of an E field with downward direction to the PMN-PT induces positive polarization charges on the surface of PMN-PT, which would extract negative charges from the BPCSO film to screen the positive polarization charges, resulting in an increase in the hole carrier density in the BPCSO film [Fig. 2(b)]. Figure 2(c) shows the polarization-electric field hysteresis loop with a remanent polarization $2P_r \sim 51\ \mu$C/cm^2 for the PMN-PT substrate. The full switching of the polarization direction is also evidenced by the box-in-box piezoresponse force microscopy images within the two green boxes, which exhibits uniform and sharp contrast between the two nonvolatile polarization states. As a result, we obtained a resistance-electric field hysteresis loop for the 16-nm BPCSO film upon the application of a bipolar E field to the PMN-PT [Fig. 2(d)], which indicates the ferroelectric-field-effect-dominated mechanism and p-type nature of the charge carriers in the BPCSO film. It is noted that the resistance is unstable with increasing electric field from 0 to +7 kV/cm or from 0 to −7kV/cm, which may related to the converse piezoelectric effect of the PMN-PT and the defects in the BPCSO film. With increasing electric fields in-plane compressive strains would be induced in the PMN-PT due to the converse piezoelectric effect. The induced strain would be transferred to the epitaxial BPCSO film, thereby influencing the strain state and resistance of the BPCSO film. On the other hand, the defects in the BPCSO film would have an impact on the screening charges at the interface region, as have been reported in $TiO_{2-\delta}$/PMN-PT structures [13]. The coactions of these two effects may result in the unstable resistance behaviors. The high and low resistance state at $E = 0$ kV/cm is marked as "$R(P_r^+)$" and "$R(P_r^-)$" states, which corresponds to the hole carrier depletion and accumulation states of the BPCSO film, respectively. As a result of the nonvolatile interfacial charge effects, the resistance for the positively polarized P_r^+ is significantly larger than that for the negatively

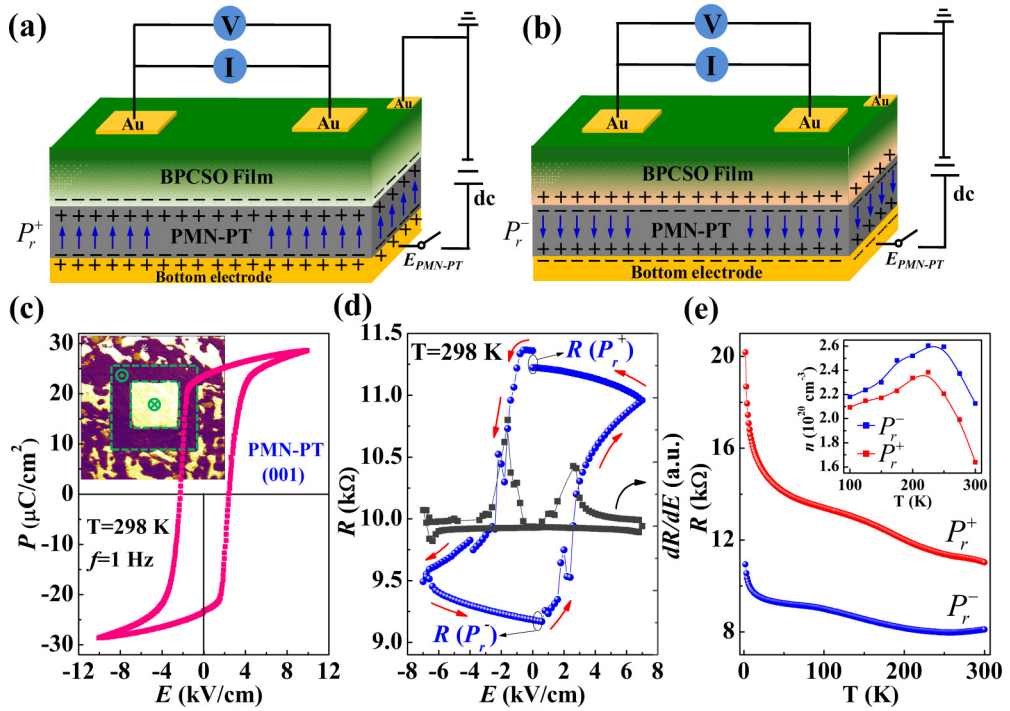

FIG. 2. Electronic transport properties of the 16-nm BPCSO thin film. [(a) and (b)] Schematic illustrations of the modification of hole carrier density of the BPCSO channel by ferroelectric gating. (c) Polarization-electric field hysteresis loop for the PMN-PT substrate. Inset shows a box-in-box piezoresponse force microscopy image of the PMN-PT under positively polarized P_r^+ (inner box) and negatively polarized P_r^- (outer box) states. (d) Resistance of the BPCSO film vs bipolar E field applied to the PMN-PT (left axis) and the corresponding dR/dE vs E (right axis) curve. (e) Temperature dependence of the resistance of the BPCSO film for the P_r^+ and P_r^- states of the PMN-PT, respectively. Inset shows the temperature dependence of the volume hole carrier density of the BPCSO film for the P_r^+ and P_r^- states of the PMN-PT, respectively.

polarized P_r^- states in the whole temperature region [Fig. 2(e)]. Hall measurements show that the hole carrier density for the P_r^+ state is smaller than that for the P_r^- state [inset of Fig. 2(e)]. All these polarization-switching-induced electronic behaviors are consistent with the ferroelectric field effect.

We adopted two kinds of magnetotransport measurement geometries [Figs. 3(c) and 3(d)] to probe into the anticipated 2D electronic transport for such a unique NMQW structure which has been confirmed by the steplike optical absorption spectra in LnCuChO (Ln = La, Pr, Nd; Ch = S, Se) [3,20] compounds that have the same layered structure as that of the BPCSO. For the relatively thicker 40-, 120-, and 160-nm BPCSO films, positive magnetoresistance (MR) with a paraboliclike shape is observed for $T = 2$, 5, 10, 20, 30 K, regardless of the polarization states of PMN-PT and the directions of the magnetic field **B** (see Ref. [19]). While for the thinnest 16 nm BPCSO film, rather complicated MR behaviors are observed (see Ref. [19]), which will be discussed in detail in the following sections. It is noteworthy that the MR versus **B** curves for $T = 2\,\mathrm{K}$ show dips at $B = 0\,\mathrm{T}$ for all films (16, 40, 120, 160 nm). This is a signature of WAL effect which usually occurs in 2D electron transport systems and manifests itself as a dip in the magnetoresistance or a sharp cusp in the magnetoconductance change $\Delta G_{(B,T)}, \Delta G_{(B,T)} = G_{(B,T)} - G_{(0,T)}$ and $G = 1/R$, within low-field region [21–23]. Hereafter, we mainly focus on the effects of the direction and strength of magnetic field as well as the polarization states of the PMN-PT on the magnetotransport behaviors and WAL effect of the thinnest 16 nm BPSCO film.

We present the measured MR of the 16-nm BPCSO film (see Ref. [19]) in the form of quantized $\Delta G(e^2/h)$ where e and h are the unit of electric charge and Planck constant, respectively. Figures 3(a), 3(b), 3(e), and 3(f) show ΔG as a function of **B** for both polarization states of the PMN-PT, as measured at different fixed temperatures. For the P_r^- state, when the direction of **B** is perpendicular to the ab plane of the film ($\mathbf{B} \perp ab$) [Fig. 3(a)], ΔG is negative and shows sharp cusps in the low-field region ($-1\,\mathrm{T} \leqslant B \leqslant 1\,\mathrm{T}$) for $T = 2$, 5, 10, 20, 30 K, which is a characteristic feature of WAL effect and may originate from the spin-orbital coupling (SOC) in the $(Cu_2Se_2)^{2-}$ layers [20,24]. Note that similar ΔG behaviors due to the WAL effect have been observed in a number of material systems, such as topological insulators [21], transition metal dichalcogenides [23], quantum well structures [25], and quantum dots [26]. In higher magnetic fields (e.g., $\mathbf{B} > 2.4\,\mathrm{T}$ for $T = 2\,\mathrm{K}$), ΔG increases with increasing **B** ($d\Delta G/dB > 0$). As a result, the sign of $d\Delta G/dB$ changes from negative to positive, implying a magnetic-field-driven crossover from WAL to WL. Furthermore, with increasing temperature from 2 to 30 K, the magnitude of the negative ΔG is significantly reduced and disappears for $T = 50$ and 100 K, indicating a suppression of the WAL effect with increasing temperature. Namely, the BPCSO film evolves from WAL dominated magnetoconductance at $T = 2\,\mathrm{K}$ to WL dominated magnetoconductance at higher temperatures, a phenomenon similar to that observed in GaAs quantum dots [26], $GaAs/In_xGa_{1-x}As/GaAs$ quantum wells [27], $Al_xGa_{1-x}N/GaN$ 2D electron gas [28], and n-InSb thin films [29].

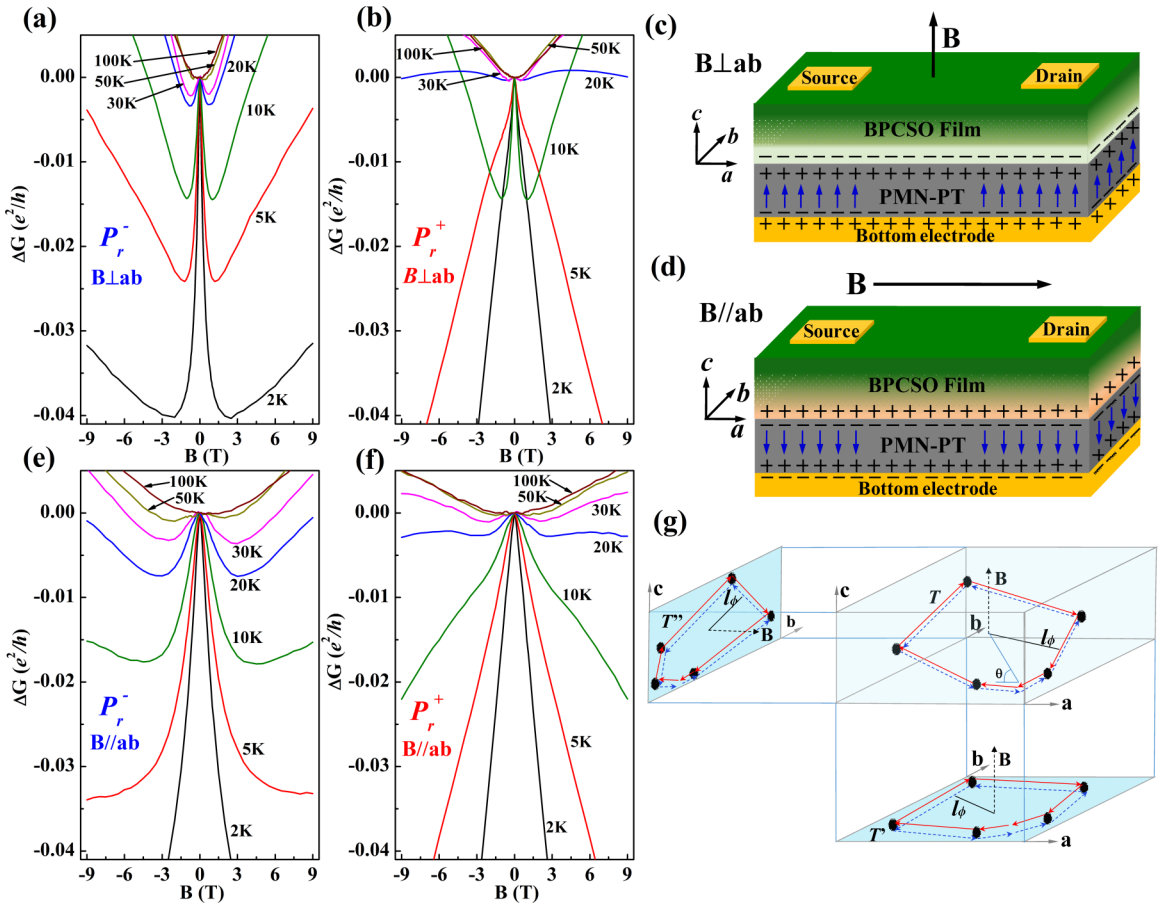

FIG. 3. Magnetoconductance change, ΔG, as a function of magnetic field **B** for the 16-nm BPCSO film. [(a), (b), (e), and (f)] ΔG of the BPCSO film for the P_r^+ and P_r^- states of the PMN-PT and different directions of the magnetic field, as measured at $T = 2, 5, 10, 20, 30, 50$, and 100 K, respectively. [(c) and (d)] Schematic illustrations of the measurement geometries with the direction of the magnetic field perpendicular and parallel to the film plane. (g) A phenomenological picture to understand the anisotropic magnetotransport behaviors.

As the polarization state is switched from P_r^- to P_r^+ [Fig. 3(b)], the low-field ΔG is still negative at low temperatures ($T = 2$, 5, 10, 20, 30 K) and positive at higher temperatures ($T = 50$, 100 K). However, the cusps of ΔG are not as sharp as that for the P_r^- state. Particularly, the negative cusps almost disappear for $T = 20$ and 30 K. This polarization-switching-induced weakening of WAL effect indicates that a higher carrier density favors WAL while a lower carrier density favors WL, similar to that observed in the GaAs/AlGaAs 2D electron gas [22]. When the direction of **B** is parallel to the ab plane (**B** $\parallel ab$) [Figs. 3(e) and 3(f)], similar ΔG behaviors are observed excepted that the sharpness of the cusps are remarkably reduced, as compared with the situation for **B** $\perp ab$, suggesting significantly weakened quantum interference correction to the conductance. All these magnetotransport behaviors suggest strong competition between WAL and WL, which is closely related to the direction and strength of magnetic field as well as the polarization states of PMN-PT.

These anisotropic magnetotransport behaviors in the low-field region could be qualitatively understood using the phenomenological picture illustrated in Fig. 3(g). As is known, the WAL results from the destructive quantum interference of electron waves when electrons are scattered in two time-reversed paths in the presence of significant SOC while the WL results from the constructive quantum interference in the absence of significant SOC [30,31]. For the BPCSO with 2D electron transport characteristics, it is assumed that the angle between the time-reversed path T and the film plane is θ. When **B** $\perp ab$ (or **B** $\parallel ab$), the effective components of T is the T' (or T''), which is the perpendicular projection of T onto the ab (or bc) plane, because the phase factor $\beta(\beta = e\Phi/\hbar)$ depends on the effective magnetic flux Φ that passes through the loop T [31], as schematically illustrated in Fig. 3(g). In 2D limit (i.e., $\theta = 0^\circ$), WAL would be the strongest when **B** $\perp ab$ and disappears when **B** $\parallel ab$, which indeed has been observed in 2D electron gas (e.g., $Al_xGa_{1-x}N/AlN/GaN$) [32] and 1D nanowires (e.g., InAs nanowires) [33]. For the present 16-nm BPCSO film the observed low-field anisotropic magnetoconductance suggests the 2D electronic transport characteristics. The appearance of WAL effect for **B** $\parallel ab$ could be ascribed to the presence of the titled interface layer, as observed in the HRTEM image [Fig. 1(h)], which would result in the effective component T''.

To quantitatively understand the low-field WAL and anisotropic magnetotransport with 2D characteristics, we invoke the Hikami-Larkin-Nagaoka (HLN) model which has been successfully used to characterize the WAl effect in 2D

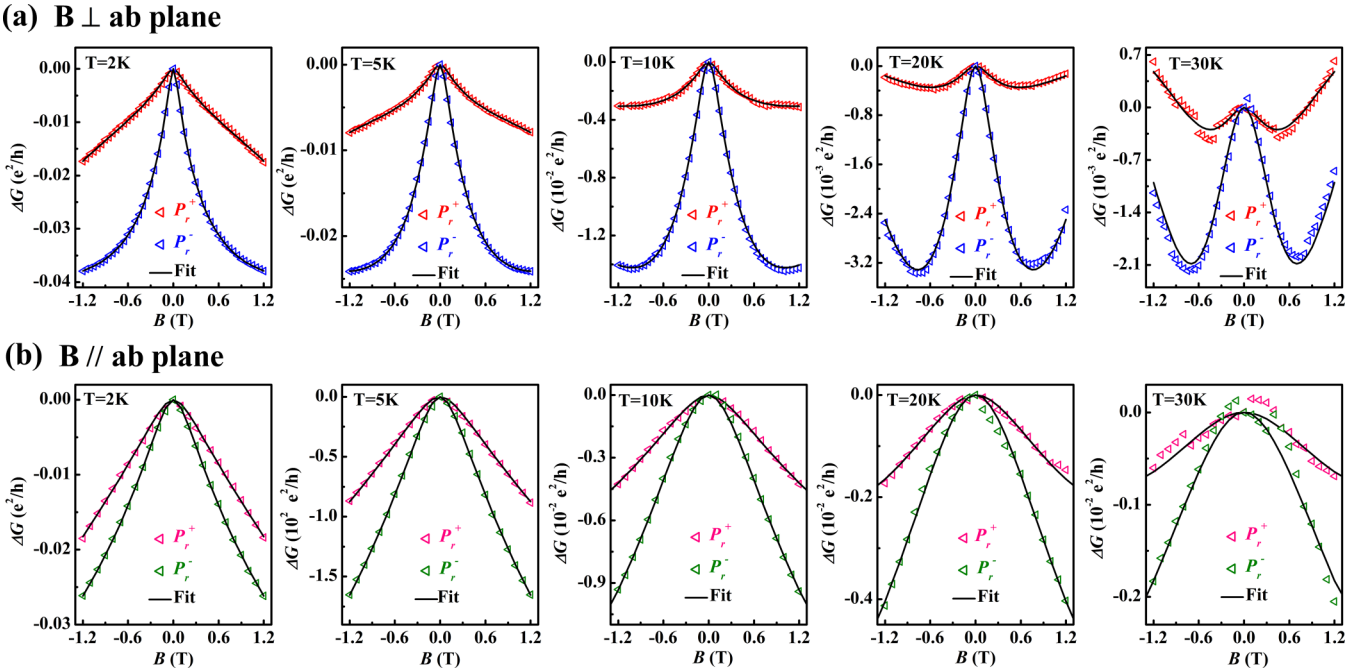

FIG. 4. HLN fitting of the low-field magnetoconductance of the 16-nm BPCSO film. (a) ΔG as a function of the magnetic field **B** for the P_r^+ and P_r^- states of the PMN-PT and **B** $\perp ab$ plane of the BPCSO film. (b) ΔG as a function of the magnetic field B for the P_r^+ and P_r^- states of the PMN-PT and **B** $\parallel ab$. The black solid lines are the fitting results.

electron transport systems [21]. We fitted the ΔG data to the HLN expression [34],

$$\Delta G = \frac{\alpha e^2}{2\pi^2\hbar}\left[f\left(\frac{B_e + B_{\rm SO} + B_{\rm S}}{B}\right) - \frac{3}{2} f\left(\frac{\frac{4}{3}B_{\rm SO} + \frac{2}{3}B_{\rm S} + B_{\rm i}}{B}\right) + \frac{1}{2} f\left(\frac{2B_{\rm S} + B_{\rm i}}{B}\right)\right], \tag{1}$$

where α is a prefactor, $f(x) = \ln(x) - \psi(1/2 + x)$, ψ is the digamma function. $B_{\rm e}$, $B_{\rm so}$, $B_{\rm s}$, and $B_{\rm i}$ are the characteristic fields for elastic scattering, spin-orbit, magnetic spin-flip, and inelastic scattering, respectively. The characteristic field B_n ($n = e$, so, s, i) is related with the characteristic length ℓ_n and time τ_n through the equation $B_n = \hbar/(4e\ell_n^2) = \hbar/(4eD\tau_n)$, where $\hbar$ and D are the reduced Planck constant and diffusion constant, respectively. Since the BPCSO film is a nonmagnetic semiconductor (see Ref. [19]), it is reasonable that there is no magnetic spin-flip scattering, resulting in $B_{\rm s} = 0$. Hall measurements show that the elastic mean free path for hole carriers (ℓ_e) is rather smaller ($\ell_e <$ 1nm, see Ref. [19]), resulting in a large $B_{\rm e}$ (>41 T) according to $B_{\rm e} = \hbar/(4e\ell_e^2)$. Under such a circumstance [i.e., $B_{\rm s} = 0$, $B_{\rm e} >$ 41 T, and $B \leqslant$ 1.2 T (fitting region)], the contribution of $f(\frac{B_e+B_{\rm so}+B_{\rm s}}{B})$ to ΔG is very weak (see Supplemental Material [19]) and could be neglected during the fitting process. Note that the inelastic and magnetic spin-flip scatterings contribute to quantum dephasing, resulting in the dephasing rate $\tau_\phi^{-1} = \tau_{i\phi}^{-1} + 2\tau_{s\phi}^{-1}$, and dephasing field $B_\phi = \hbar/(4eD\tau_\phi) = B_i + 2B_s$. Similar to the way that was employed to fit the ΔG of the layered Nb_3SiTe_6 single crystals [35], the classical orbital MR ($\propto B^2$) due to the Lorentz force is also considered during the fitting. As shown in Figs. 4(a) and 4(b), ΔG at five fixed temperatures (T = 2, 5, 10, 20, and 30 K) for both the P_r^+ and P_r^- states of the PMN-PT can be quite well fitted using Eq. (1) in the low-field region (1.2 T $\leqslant$ **B** $\leqslant$ 1.2 T) whether **B** is perpendicular [Fig. 4(a)] or parallel [Fig. 4(b)] to the ab plane of the BPCSO. The dephasing field B_ϕ is extracted from the fitting to further understand the anisotropic electronic properties.

Figure 5(a) shows the temperature dependence of B_ϕ for both the P_r^+ and P_r^- states of the PMN-PT. Whether **B** $\perp ab$ or **B** $\parallel ab$, B_ϕ for both polarization states increases with increasing temperature, suggesting stronger inelastic scattering at higher temperatures. A noticeable anisotropy of B_ϕ can be observed once the direction of the magnetic field changes from **B** $\perp ab$ to **B** $\parallel ab$. For **B** $\parallel ab$, the temperature-dependent B_ϕ shows almost no difference between the P_r^+ and the P_r^- states. However, for **B** $\perp ab$, B_ϕ show appreciable difference between the P_r^+ and the P_r^- states at high temperatures ($T \geqslant$ 30 K). Using the phenomenological picture shown in Fig. 3(g), these phenomena can be reasonably understood. Since the BPCSO film has a 2D electronic transport characteristic, a stronger phase coherence of charge carriers is expected in the ab plane with respect to that in the bc plane because T' in the ab plane is pretty larger than T'' in the bc plane. As a result, a smaller B_ϕ or a larger phase coherence length ℓ_ϕ would be obtained for **B** $\perp ab$. This is indeed consistent with the experimental results shown in Figs. 5(a) and 5(b) where both B_ϕ and ℓ_ϕ show strong anisotropy. Further, ℓ_ϕ shows a crossover around 6 K between the P_r^+ and the P_r^- states, implying a competition between the electron-electron scattering dominated dephasing mechanism ($T <$ 6 K) and the electron-phonon scattering dominated dephasing mechanism ($T >$ 6 K). The dephasing rate τ_ϕ^{-1}, which controls the magnitude and temperature dependence of the quantum interference effect, can be described by the

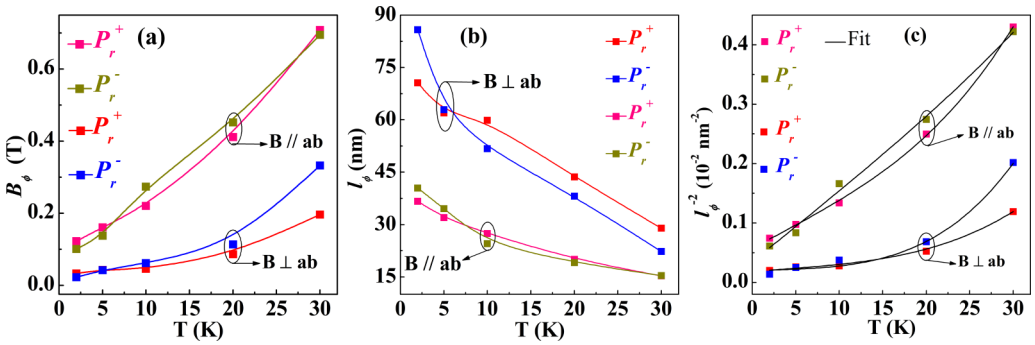

FIG. 5. Fitting parameters of the low-field magnetoconductance for the 16-nm BPCSO film. (a) Temperature dependence of the dephasing field B_ϕ for the P_r^+ and P_r^- states of the PMN-PT when $\mathbf{B} \perp ab$ and $\mathbf{B} \parallel ab$. (b) Temperature dependence of the dephasing length ℓ_ϕ for the P_r^+ and P_r^- states of the PMN-PT when $\mathbf{B} \perp ab$ and $\mathbf{B} \parallel ab$. (c) Fitting of ℓ_ϕ^{-2} using Eq. (4) for the P_r^+ and P_r^- states of the PMN-PT when $\mathbf{B} \perp ab$ and $\mathbf{B} \parallel ab$.

following expression for nonmagnetic semiconductors [36],

$$\tau_\phi^{-1} = \tau_0^{-1} + \tau_{\phi,e-e}^{-1} + \tau_{\phi,e-\mathrm{ph}}^{-1}, \tag{2}$$

where τ_0^{-1} is the finite zero temperature dephasing rate, $\tau_{\phi,e-e}^{-1}$ and $\tau_{\phi,e-\mathrm{ph}}^{-1}$ represent the dephasing rate caused by inelastic electron-electron and electron-phonon scatterings, respectively. Given that both of the inelastic scatterings from the electron-electron and electron-phonon interactions yield a power law term in the temperature dependence of dephasing rate, the total dephasing rate can be rewritten as [35,36],

$$\tau_\phi^{-1} = \tau_0^{-1} + \mathrm{a}T^{P_{e-e}} + bT^{P_{e-\mathrm{ph}}}, \tag{3}$$

where $\mathrm{a}T^{P_{e-e}}$ and $bT^{P_{e-\mathrm{ph}}}$ are the contributions from inelastic electron-electron and electron-phonon scatterings, respectively. Since $\hbar/(4e\ell_n^2) = \hbar/(4eD\tau_n)$ and it is quite difficult to obtain the diffusion constant D of the 16 nm BPCSO film, Eq. (3) is thus expressed in the form of ℓ_ϕ^{-2} through the following equation:

$$\ell_\phi^{-2} = A + BT^{P_{e-e}} + CT^{P_{e-\mathrm{ph}}}, \tag{4}$$

where A, B, and C are prefactors that are related to the diffusion constant D. Typically, the electron-electron scattering dominates the low temperature dephasing for 1D and 2D systems, with the exponent $P_{e-e} \approx 2/3$ and 1 for 1D and 2D systems [36], respectively. In contrast, the electron-phonon scattering dominates the dephasing for 3D systems, but contributes much less at lower dimensions, with the exponent $P_{e-\mathrm{ph}}$ varying from 2 to 4 for all dimensions [36]. Using $P_{e-e} = 1$ and $P_{e-\mathrm{ph}} = 3.5$, we obtain good fitting of ℓ_ϕ^{-2} to Eq. (4) [Fig. 5(c)] and summarize the fitting parameters in Table I. The weight of electron-electron interaction (or equivalently, the prefactor B) is approximately four orders of magnitude larger than that of the electron-phonon interaction (the prefactor C), implying that the electron-electron interaction plays the dominant role at low temperatures (few degrees Kelvin). For example, for the $\mathbf{B} \perp ab$ and P_r^- state, the calculated values of $BT^{P_{e-e}}$ and $CT^{P_{e-\mathrm{ph}}}$ at $T = 6\,\mathrm{K}$ are 2.56×10^{-4} and $0.60 \times 10^{-4}\,\mathrm{nm}^{-2}$, respectively. The contribution from the latter is only 23.4% of that from the former. We note that the polarization switching from P_r^+ and P_r^- (or from P_r^- and P_r^+) has significant impact on the prefactors B and C, which highlights the advantage of using ferroelectric gating to study the relative importance of carrier density on the electron-electron and electron-phonon interactions in reduced dimensions.

IV. SUMMARY

In summary, we report the fabrication of ZrCuSiAs-type copper oxyselenide thin films on ferroelectric PMN-PT single crystals to form ferroelectric field effect devices in which the carrier density, resistance, magnetoconductance, coherence length of carriers, and the dephasing rate and dephasing field of the films could be reversibly manipulated in a nonvolatile manner by the polarization switching at room temperature. Systematical magnetic field direction, polarization state, and temperature dependent magnetotransport measurements reveal strong competition between the weak antilocalization and weak localization and support the 2D electronic transport properties of the BPCSO film at low temperatures. Based on the quantum interference, a phenomenological picture is adopted to understand the anisotropic low-field magnetoconductance.

TABLE I. Parameters of electron-electron scattering and electron-phonon scattering obtained from the fitting of ℓ_ϕ^{-2} using Eq. (4). $\Delta A, \Delta B$, and ΔC are the difference of the values of parameters A, B, and C by the polarization reversal.

		A ($10^{-4}\,\mathrm{nm}^{-2}$)	B ($10^{-5}\,\mathrm{nm}^{-2}\,\mathrm{K}^{-1}$)	C ($10^{-9}\,\mathrm{nm}^{-2}\,\mathrm{K}^{-3.5}$)
$\mathbf{B} \perp$ ab	P_r^+	1.851	1.044	4.701
	P_r^-	1.980	0.427	11.340
	$\Delta A, \Delta B, \Delta C$	–0.129	0.617	–6.639
$\mathbf{B} \parallel$ ab	P_r^+	5.734	7.799	9.415
	P_r^-	3.465	11.890	2.009
	$\Delta A, \Delta B, \Delta C$	2.269	–4.091	7.406

Our results not only offer an in-depth understanding of the low-temperature electronic properties of BCSO-based compounds but also provide a promising step toward exploring thermoelectric/ferroelectric hybrid devices and a simple and straightforward approach to realize reversible and nonvolatile tuning of electronic properties of ZrCuSiAs-type copper oxyselenide thin films.

ACKNOWLEDGMENTS

This work was supported by the National Natural Science Foundation of China (Grant Nos. 51572278, 51790491, 51502129), the National Basic Research Program of China (Grant Nos. 2016YFA0300103 and 2015CB921201), and the Chinese Academy of Sciences (Grant No. KGZD-EW-T06).

X.-W.Z. and G.-Y.G. contributed equally to this work.

[1] Y. Kamihara, T. Watanabe, M. Hirano, and H. Hosono, J. Am. Chem. Soc **130**, 3296 (2008).

[2] K. Ueda, S. Inoue, S. Hirose, H. Kawazoe, and H. Hosono, Appl. Phys. Lett. **77**, 2701 (2000).

[3] K. Ueda, H. Hiramatsu, M. Hirano, T. Kamiya, and H. Hosono, Thin Solid Films **496**, 8 (2006).

[4] V. V. Bannikov and A. L. Ivanovskii, J. Struct. Chem. **56**, 148 (2015).

[5] C. Krellner, N. S. Kini, E. M. Brüning, K. Koch, H. Rosner, M. Nicklas, M. Baenitz, and C. Geibel, Phy. Rev. B **76**, 104418 (2007).

[6] X. X. Li, X. J. Wu, and J. L. Yang, J. Mater. Chem. C **1**, 7197 (2013).

[7] J. H. Sui, J. Li, J. Q. He, Y. L. Pei, D. Berardan, H. J. Wu, N. Dragoe, W. Cai, and L. D. Zhao, Energy Environ. Sci. **6**, 2916 (2013).

[8] J. L. Lan, Y. C. Liu, B. Zhan, Y. H. Lin, B. P. Zhang, X. Yuan, W. Q. Zhang, W. Xu, and C. W. Nan, Adv. Mater. **25**, 5086 (2013).

[9] Y. L. Pei, J. Q. He, J. F. Li, F. Li, Q. J. Liu, W. Pan, C. Barreteau, D. Berardan, N. Dragoe, and L. D. Zhao, NPG Asia Mat. **5**, e47 (2013).

[10] L. D. Zhao, D. Berardan, Y. L. Pei, C. Byl, L. Pinsard-Gaudart, and N. Dragoe, Appl. Phys. Lett. **97**, 092118 (2010).

[11] C. Z. Chang, Z. C. Zhang, K. Li, X. Feng, J. S. Zhang, M. H. Guo, Y. Feng, J. Wang, L. L. Wang, X. C. Ma, X. Chen, Y. Y. Wang, K. He, and Q. K. Xue, Nano Lett. **15**, 1090 (2015).

[12] C. H. Ahn, S. Gariglio, P. Paruch, T. Tybell, L. Antognazza, and J. M. Triscone, Science **284**, 1152 (1999).

[13] L. Chen, W. Y. Zhao, J. Wang, G. Y. Gao, J. X. Zhang, Y. Wang, X. M. Li, S. X. Cao, X. G. Li, H. S. Luo, and R. K. Zheng, ACS Appl. Mater. Interfaces **8**, 26932 (2016).

[14] Q. X. Zhu, M. M. Yang, M. Zheng, R. K. Zheng, L. J. Guo, Y. Wang, J. X. Zhang, X. M. Li, H. S. Luo, and X. G. Li, Adv. Funct. Mater. **25**, 1111 (2015).

[15] A. Rajapitamahuni, J. Hoffman, C. H. Ahn, and X. Hong, Nano Lett. **13**, 4374 (2013).

[16] M. Liu, O. Obi, J. Lou, Y. J. Chen, Z. H. Cai, S. Stoute, M. Espanol, M. Lew, X. D. Situ, K. S. Ziemer, V. G. Harris, and N. X. Sun, Adv. Funct. Mater. **19**, 1826 (2009).

[17] J. Ravichandran, C. R. Serrao, D. K. Efetov, D. Yi, Y. S. Oh, S.-W. Cheong, R. Ramesh, and P. Kim, J. Phys.: Condens Matter **28**, 505304 (2016).

[18] L. D. Zhao, J. Q. He, D. Berardan, Y. H. Lin, J. F. Li, C. W. Nan, and N. Dragoe, Energy Environ. Sci. **7**, 2900 (2014).

[19] See Supplemental Material at http://link.aps.org/supplemental/10.1103/PhysRevMaterials.2.055003 for the calculation of electric-field-induced areal charge density changes, XRD rocking curve, TEM images, simulated electron diffraction pattern, magnetoresistance, magnetic hysteresis loops, elastic mean free path, and $f(\frac{B_e+B_{so}+B_s}{B})$ values.

[20] K. Ueda, H. Hiramatsu, H. Ohta, M. Hirano, T. Kamiya, and H. Hosono, Phy. Rev. B **69**, 155305 (2004).

[21] M. H. Liu, J. S. Zhang, C. Z. Chang, Z. C. Zhang, X. Feng, K. Li, K. He, L. L. Wang, X. Chen, X. Dai, Z. Fang, Q. K. Xue, X. C. Ma, and Y. Y. Wang, Phys. Rev. Lett. **108**, 036805 (2012).

[22] J. B. Miller, D. M. Zumbuhl, C. M. Marcus, Y. B. Lyanda-Geller, D. Goldhaber-Gordon, K. Campman, and A. C. Gossard, Phys. Rev. Lett. **90**, 076807 (2003).

[23] E. Z. Zhang, R. Chen, C. Huang, J. H. Yu, K. T. Zhang, W. Y. Wang, S. S. Liu, J. W. Ling, X. G. Wan, H. Z. Lu, and F. X. Xiu, Nano Lett. **17**, 878 (2017).

[24] H. Chi, H. Kim, J. C. Thomas, G. S. Shi, K. Sun, M. Abeykoon, E. S. Bozin, X. Y. Shi, Q. Li, X. Shi, E. Kioupakis, A. Van der Ven, M. Kaviany, and C. Uher, Phys. Rev. B **89**, 195209 (2014).

[25] T. Koga, J. Nitta, T. Akazaki, and H. Takayanagi, Phys. Rev. Lett. **89**, 046801 (2002).

[26] D. M. Zumbuhl, J. B. Miller, C. M. Marcus, K. Campman, and A. C. Gossard, Phys. Rev. Lett. **89**, 276803 (2002).

[27] G. M. Minkov, A. V. Germanenko, O. E. Rut, A. A. Sherstobitov, L. E. Golub, B. N. Zvonkov, and M. Willander, Phys. Rev. B **70**, 155323 (2004).

[28] N. Thillosen, S. Cabañas, N. Kaluza, V. A. Guzenko, H. Hardtdegen, and Th. Schäpers, Phys. Rev. B **73**, 241311(R) (2006).

[29] R. L. Kallaher and J. J. Heremans, Phys. Rev. B **79**, 075322 (2009).

[30] B. L. Altshuler and A. G. Aronov, in *Electron-electron Interactions in Disordered Systems*, edited by A. L. Efros and M. Pollak (Elsevier, Amsterdam, 1985).

[31] M. Brahlek, N. Koirala, N. Bansal, and S. Oh, Solid State Commun. **215**, 54 (2015).

[32] C. Kurdak, N. Biyikli, Ü. Özgür, H. Morkoç, and V. I. Litvinov, Phys. Rev. B **74**, 113308 (2006).

[33] P. Roulleau, T. Choi, S. Riedi, T. Heinzel, I. Shorubalko, T. Ihn, and K. Ensslin, Phys. Rev. B **81**, 155449 (2010).

[34] S. Hikami, A. I. Larkin, and Y. Nagaoka, Prog. Theor. Phys. **63**, 707 (1980).

[35] J. Hu, X. Liu, C. L. Yue, J. Y. Liu, H. W. Zhu, J. B. He, J. Wei, Z. Q. Mao, L. Y. Antipina, Z. I. Popov, P. B. Sorokin, T. J. Liu, P.W. Adams, S. M. A. Radmanesh, L. Spinu, H. Ji, and D. Natelson, Nat. Phys. **11**, 471 (2015).

[36] J. J. Lin and J. P. Bird, J. Phys.: Condens. Matter **14**, R501 (2002).